Hierarchical Frequency and SOC Control of Power Grids With Battery Energy Storage Systems

Zakaria Afshar, *Student Member, IEEE*, Indra Bhogaraju, Hamid Rahmanei, and Mehdi Farasat, *Senior Member, IEEE*

***Abstract*—A novel approach to modeling of and integrating the state-of-charge (SOC) of a battery energy storage system (BESS) into the load frequency control of power systems is proposed. By considering the SOC as a state variable in the state-space model of the system, a hierarchical frequency and SOC control scheme is introduced. On top of the primary frequency control, which is the lowest hierarchy level, the SOC signal is used as the input to a novel primary charge controller (PCC) to prevent the BESS from discharging/charging beyond minimum/maximum allowable ranges. In the middle level of the hierarchy, the secondary frequency control loop is augmented to restore the system frequency to its nominal value when the PCC is active. At the top level of the hierarchy, a novel secondary charge controller (SCC) is designed to charge the BESS to its maximum allowable range so that it can continue to contribute to frequency control. System stability is studied using Popov/circle criterion. It is also shown that with multiple distributed energy storage units, following the SOC-balancing principle and by sharing SOC information among the units, only one BESS shall be equipped with the proposed PCC and SCC. Effectiveness of the proposed hierarchical control in providing fast and stable frequency response under different load and generation conditions is validated through hardware-in-the-loop studies.**

***Index Terms*—Battery energy storage systems, frequency control, hierarchical control, SOC control.**

I. Introduction

LOAD frequency control (LFC) of the power system is crucial when there is an imbalance between active power generation and demand [1]; a surplus in generation leads to increased frequency and a deficit causes frequency drop. Primary frequency control (PFC) in power systems adjusts the operating point of prime movers and consequently, the synchronous generators response to such frequency fluctuations. To eliminate the frequency response error of the PFC, a secondary frequency control (SFC), also known as automatic generation control, is applied in the power system. In SFC, which is performed in some control areas that monitor the grid frequency, the measured frequency is passed through an integral controller and the corresponding generated reference power is obtained and sent to the generation units via communication links to eliminate the steady-state error.

With higher integration of renewable energy systems and electric vehicles (EVs) to the power system, recent studies have proposed modifications to the traditional LFC model of the power system. Some papers have included the comprehensive model of wind turbine generation [2] and photovoltaic systems [3], as disturbances in the LFC model. In [4] and [5], EVs are modeled along with the LFC model by taking vehicle-to-grid technology into consideration. In [6], demand response is modeled within LFC. Communication link delays in SFC are considered and coped with in [7] and [8]. In some papers, such as [9] and [10], PFC and SFC are not distinguished within LFC. In [11], although PFC and SFC are distinguished, the time frames associated with each control layer are not considered. As explained in [12], PFC response time is to the extent of seconds whereas SFC response time ranges from tens of seconds (20 to 30 s) to minutes. Advanced controllers, such as robust H-infinity controller [9], [13], intelligent controllers [14], and fractional order controller [15], have been employed to replace the conventional integral controller in the SFC loop. However, these controllers are complicated for real-time implementation.

In [9], [10], and [11], BESS is added to the LFC model of a conventional power system. Although this model is widely used for a single-area power system with a synchronous generator (SG) and a BESS, it can be extended to two-area or larger power systems as well. Also, this extended LFC model is commonly used for islanded microgrids or shipboard power systems with a diesel generator and a BESS. The BESS can practically contribute to inertial response [16], [17] and also to PFC [18]. Although BESS can be theoretically used for SFC, as used in [19], it is, however, impractical to consider it for this purpose due to its low capacity compared to SG units. More importantly, the battery SOC must be considered and controlled while it contributes to PFC. Otherwise, once the BESS depletes and ceases power injection to the grid, there will be a sudden loss of source of generation and a rapid frequency drop. This may trigger the rate-of-change-of-frequency (ROCOF) relays within the power system if the SG units could not ramp up

Manuscript received 27 July 2023; revised 10 November 2023 and 30 January 2024; accepted 17 March 2024. Date of publication 29 March 2024; date of current version 16 May 2024. An earlier version of this article was presented in part at the 2023 IEEE Texas Power and Energy Conference (TPEC) [DOI: 10.1109/TPEC56611.2023.10078647]. Recommended for publication by Associate Editor M. Saeedifard. *(Corresponding author: Mehdi Farasat.)*

Zakaria Afshar is with the Division of Electrical and Computer Engineering, Louisiana State University, Baton Rouge, LA 70803 USA.

Indra Bhogaraju is with ABB Corporate Research, Raleigh, NC 27606 USA.

Hamid Rahmanei is with the Department of Mechanical Engineering, K. N. Toosi University of Technology, Tehran, Iran.

Mehdi Farasat is with the Division of Electrical and Computer Engineering, Louisiana State University, Baton Rouge, LA 70803 USA (e-mail: mfarasat@lsu.edu).

Color versions of one or more figures in this article are available at https://doi.org/10.1109/TPEL.2024.3383293.

Digital Object Identifier 10.1109/TPEL.2024.3383293

their generation quickly. This issue is not considered in [20], for instance. There, to prevent power draw/injection from/to the BESS, a logic-based method is used to set the reference current in the BESS's inverter control to zero when its SOC reaches the minimum/maximum allowable range. Our comparative study shows that frequency deviations and oscillations are more severe under this method.

Very few studies have attempted to model and control the battery SOC in LFC. In [21] and [22], the SOC is controlled by some logic-based (if/then) algorithms, and the SOC is not modeled as part of the system dynamics. This makes system stability analysis difficult, as such studies are not presented in [22]. In [24] and [25], SOC-based adaptive droop controllers are proposed, where the droop gain is a nonlinear function of SOC and varies such that as SOC nears its allowable range, the BESS charge/discharge slows down. Like [22], stability analysis of these methods is not presented.

In case of multiple BESSs, it is conventional to follow an SOC-balancing approach for minimizing the number of charge/discharge cycles of the BESSs. In [23], a multiagent-based distributed control is proposed to achieve SOC balancing using dynamic average consensus; however, frequency restoration and recharge control of the BESSs have not been investigated. In [26], an adaptive virtual power concept is introduced and used along with consensus control to modify the frequency droop control formula. In [27], a method to modify the droop gain is proposed to achieve SOC balancing. Like [23], there is no recharge control method to show the SOC balancing while the BESSs are being charged to their maximum SOC. Additionally, system stability is not considered when altering the droop gains.

For frequency and SOC control, it is more rational to first model the SOC as a state variable in the state-space model of LFC, and then design a controller to maintain the SOC above a predefined lower bound to preserve the battery charge for contingency conditions, and to prevent sudden disconnection of the BESS from the grid. In [13] and [28], the BESS SOC is derived as the integral of the BESS output power. However, we showed in [29] that this is not precise and derived a proper and accurate relation. This enabled us to incorporate the SOC into the extended LFC model. Also, we designed a primary charge controller (PCC) with a closed-loop system to ensure the SOC will not drop below its lower bound. Compared to [29], in this article, we 1) improve the PCC design such that the BESS SOC is also limited to its maximum allowable range when it is charged during reduced load time intervals, 2) consider the SFC loop, investigate the new features of the SOC-aware SFC, and provide guidelines to design the secondary frequency controller in presence of the PCC, 3) propose a new piecewise linear charge controller, referred to as secondary charge controller (SCC), to charge the BESS during off-peak load time once the secondary control loop is closed and there is surplus of power, and 4) extend the proposed frequency and SOC control to a power system with multiple BESSs. System stability is investigated using the Popov/circle criterion, and guidelines for tuning the SCC parameter are presented. The correctness of the proposed model along with the proposed controllers is validated through simulations. Real-time, hardware-in-the-loop (HIL) studies are performed with different load and battery SOC to verify the effectiveness of the proposed hierarchical control in maintaining frequency of the system at its nominal value. Comparative studies are conducted to show the advantage of integrating SOC into the system model, along with frequency, and designing the controller based on the new system dynamics. In addition to comparative studies, features of the surveyed methods in this literature review are summarized and compared against the proposed method in Table I.

TABLE I
COMPARISON OF THIS WORK WITH PREVIOUS WORKS

Ref	Frequency restoration	Recharge control	Stability analysis	SOC modeled as a state variable	SOC balancing
[20]	Yes	Yes	No	No	No
[21]	Yes	No	Yes	No	No
[23]	No	No	Yes	No	Yes
[25]	No	Yes	No	No	No
[26]	Yes	No	Yes	No	Yes
[27]	No	No	No	No	Yes
[29]	No	No	Yes	Yes	No
This paper	Yes	Yes	Yes	Yes	Yes

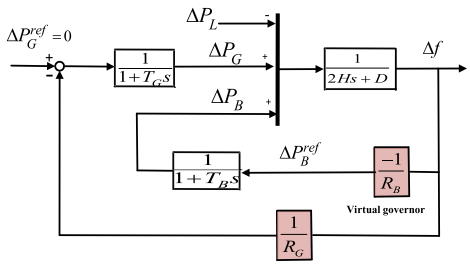

Fig. 1. Primary frequency control with BESS [8], [9], [18].

Major contributions of this article are three-fold.

1) The LFC state-space model is modified by including the BESS SOC as a state variable. Based on this model, novel primary and SCCs are designed in the primary and SFC loops to maintain the BESS charge within desired margins.
2) The primary and SCCs are designed to satisfy the Popov/circle stability criterion and are embedded as control layers in the proposed hierarchical control.
3) The proposed hierarchical frequency and SOC control is extended to a power system with multiple BESSs.

The rest of this article is organized as follows. Sections II and III discuss PFC and SFC with BESS SOC consideration, respectively, Multiple BESSs are discussed in Sections IV and V provides model validation, HIL results are presented in Sections VI. Finally, Section VII concludes this article.

II. PFC OF POWER SYSTEMS WITH BESS SOC CONSIDERATION

Fig. 1 depicts the PFC model of a power system with BESS, which is widely used in the literature [8], [9], [18]. The BESS is embedded into the LFC model to contribute to PFC by the use of a virtual governor. The virtual governor is a proportional

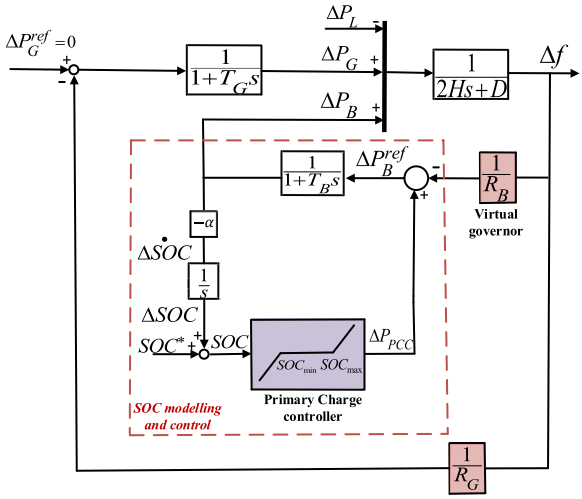

Fig. 2. SOC-aware primary frequency control.

controller with the BESS droop gain R_B, which yields the BESS reference power ΔP_B^{ref} . The BESS droop gain influences the steady-state value of frequency deviation Δf as follows:

$$\Delta f = -\Delta P_L/(D + 1/R_G + 1/R_B) \tag{1}$$

where ΔP_L is the load variation, D is the power system damping ratio, and R_G is the generator droop gain. However, the BESS can contribute to PFC only if there is available charge. Therefore, the SOC must be incorporated into this model.

In [29], we derived the following equation that relates the time derivative of battery SOC variation ΔSOC to its output power variation in per unit, $\Delta P_B^{\text{p.u.}}$

$$\frac{d}{dt}\Delta\text{SOC} = -\alpha \Delta P_B^{\text{p.u.}}, \qquad \alpha = \frac{S_{\text{base}}}{36 E_{\max}} \tag{2}$$

where S_{base} is the base apparent power and $E_{\max}$ is the maximum energy capacity of the BESS in Wh. By integrating $\frac{d}{dt}\Delta$SOC and adding it to the initial SOC percentage, SOC*, the actual value of SOC can be obtained as follows:

$$\text{SOC} = \text{SOC}^* + \Delta\text{SOC}. \tag{3}$$

Using this derivation, we were able to incorporate the SOC into PFC, as shown in Fig. 2.

The PCC in Fig. 2 is a piecewise linear controller, which is proposed to prevent the BESS SOC from dropping below/exceeding the allowable minimum/maximum values, $\text{SOC}_{\min}$ and $\text{SOC}_{\max}$, respectively. The controller produces a power reference modifier signal ΔP_{PCC} that modifies the reference power of the BESS as

$$\Delta P_{\text{PCC}} = \begin{cases} m(\text{SOC} - \text{SOC}_{\min}) & \text{SOC} < \text{SOC}_{\min} \\ 0 & \text{SOC}_{\min} \le \text{SOC} \le \text{SOC}_{\max} \\ m(\text{SOC} - \text{SOC}_{\max}) & \text{SOC} > \text{SOC}_{\max}. \end{cases} \tag{4}$$

Here, m is the slope of the linear piece of the controller. The range of this parameter is given in (7) and details about its derivation are provided in [29]. It is noteworthy to mention that although the proposed PCC in [29] only considers the lower bound of SOC and the proposed PCC in this article considers both the upper and lower bounds, they lie in the first and third quadrant of the coordinates and thus, both the controllers satisfy the Popov/circle criterion when m satisfies (7).

In [29], by using the equilibrium definition, we found that the steady-state value of BESS output power will be zero ($\Delta P_B = 0$) to prevent the SOC from decreasing. Also, there will be a frequency drop due to gradual loss of a generation source, and the SOC will settle slightly under the $\text{SOC}_{\min}$ with an error.

Following the same principle, the modified PCC will lead to a steady-state error when SOC reaches $\text{SOC}_{\max}$. The steady-state values for frequency variation and the SOC are as follows:

$$\Delta f = -\Delta P_L/(D + 1/R_G) \tag{5}$$

$$\text{SOC} = \text{SOC}_{\min} - \frac{\Delta P_L}{m R_B (D + 1/R_G)}, \quad \text{for SOC} < \text{SOC}_{\min} \text{ and } \Delta P_L > 0$$

$$\text{SOC} = \text{SOC}_{\max} - \frac{\Delta P_L}{m R_B (D + 1/R_G)}, \quad \text{for SOC} > \text{SOC}_{\max} \text{ and } \Delta P_L < 0. \tag{6}$$

Comparing (1) and (5) proves that there will be frequency drop, as $1/R_B$ is no longer present in the Δf equation. Equation (6) shows that the bigger the m is, the smaller the SOC error ($e_{\text{SOC}} = \text{SOC}_{\min} - \text{SOC}$ or $e_{\text{SOC}} = \text{SOC} - \text{SOC}_{\max}$) will be. However, the bigger values of m lead to abrupt disconnection of the BESS, thereby higher ROCOF. Also, extremely large values of m can lead to violation of the stability criteria, which we derived in [29] based on Popov/circle criterion as follows:

$$0 < m < \frac{T_B}{\alpha}\frac{a_0^2}{a_1 b_0} \tag{7}$$

where

$$a_0 = \frac{D}{2HT_BT_G} + \frac{1}{2HR_GT_BT_G} + \frac{1}{2HR_BT_BT_G}$$

$$a_1 = \frac{1}{T_BT_G} + \frac{1}{2HR_BT_B} + \frac{1}{2HR_GT_G} + \frac{D}{2H}\left(\frac{1}{T_B} + \frac{1}{T_G}\right)$$

$$b_0 = \frac{D}{2HT_G} + \frac{1}{2HR_GT_G}.$$

It is clear from (7) that a large α leads to a small slope m, and from (7), a large α corresponds to a small $E_{\max}$. This means that for a low-capacity BESS, a small slope m should be selected.

III. SFC of Power Systems by Considering the SOC

Fig. 3 depicts addition of SFC loop to the SOC-aware PFC. The secondary frequency controller is an integral controller that takes frequency variation (Δf) as the input and outputs a reference power variation (ΔP_G^{ref}) for SG units. As already mentioned, the time scale of PFC is to the extent of a few seconds, whereas SFC is applied after a few minutes. This is modeled by a switch that is closed at $t = t_{SF}$. The SFC loop is closed to the system through communication links after PFC loop is closed. The time that SFC loop is closed depends on how close the frequency deviation is to the acceptable margin. SFC loop remains in the control system until the frequency offset is eliminated and frequency is brought back to the rated value.

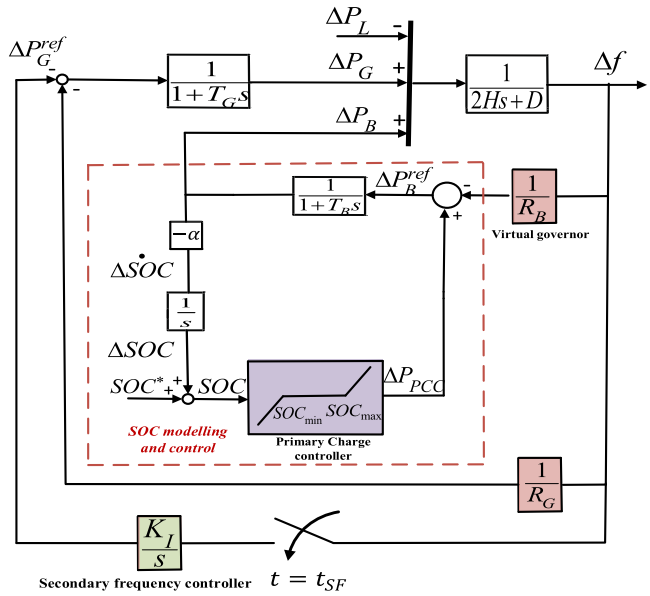

Fig. 3. SOC-aware secondary frequency control.

A. Steady-State Analysis

Following the same approach we proposed in [29], the state-space model of the system with the secondary frequency controller in the loop is derived as follows:

$$\frac{d}{dt}\Delta f = -\frac{D}{2H}\Delta f + \frac{1}{2H}\Delta P_G + \frac{1}{2H}\Delta P_B - \frac{1}{2H}\Delta P_L \tag{8}$$

$$\frac{d}{dt}\Delta P_G = -\frac{1}{T_G R_G}\Delta f - \frac{1}{T_G}\Delta P_G - \frac{1}{T_G}\Delta P_G^{ref} \tag{9}$$

$$\frac{d}{dt}\Delta P_B = -\frac{1}{T_B R_B}\Delta f - \frac{1}{T_B}\Delta P_B + \frac{1}{T_B}\Delta P_{\text{PCC}} \tag{10}$$

$$\frac{d}{dt}\Delta \text{SOC} = -\alpha \Delta P_B \tag{11}$$

$$\frac{d}{dt}\Delta P_G^{ref} = K_I \Delta f. \tag{12}$$

Using the equilibrium definition $dx/dt = 0$ for each of the state variables in (8)–(12), leads to$\Delta f = \Delta P_B = 0$. This shows that the steady-state error of the frequency response is now eliminated, and the BESS does not supply power in the steady state and the load is met by the generator ($\Delta P_G = \Delta P_L$). Moreover, $\text{SOC} = \text{SOC}_{\text{min}}$, which proves that the SOC steady-state error is eliminated.

B. Secondary Frequency Controller Design

For tuning the secondary frequency controller parameter (K_I) in conventional LFC of power systems, it is customary to neglect the time constants, i.e., $T_G = T_B = 0$, and then to design the critical controller parameter ($K_{I\,crit}$) based on the critically damped response of the system [30]. This approach leads to

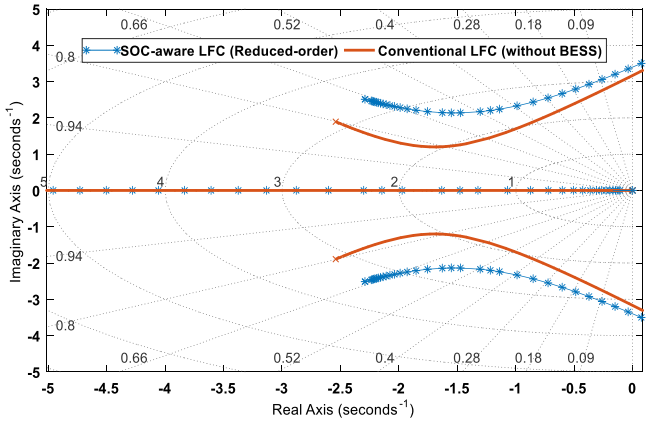

Fig. 4. Root-loci of the reduced-order SOC-aware LFC and conventional LFC without BESS.

the following equation for $K_{I\,crit}$:

$$K_{I\,crit} = \frac{1}{8H}\left(D + \frac{1}{R_G} + \frac{1}{R_B}\right)^2. \tag{13}$$

However, (13) leads to an incorrect value for $K_{I\,crit}$ when the SOC is considered in the system dynamics. This is because the PCC affects the performance of the secondary frequency controller. It is noteworthy that once the PCC has taken effect, it means that the BESS output power has reached zero. Therefore, it is reasonable to neglect the BESS dynamics in the LFC model. This reduces the model to the conventional LFC model without BESS. Thus, (13) will reduce to

$$K_{I\,crit} = \frac{1}{8H}\left(D + \frac{1}{R_G}\right)^2. \tag{14}$$

To evaluate the impact of system model simplification and accuracy of (14), the root-locus of the proposed SOC-aware LFC system is compared to that of the conventional LFC system without the BESS model. Residualization method is used to reduce the order of the proposed system as it is of order of five, whereas the order of the conventional LFC system is three. In this method, the time derivative of the state variables that are supposed to be eliminated are set to zero. For the proposed system, we consider the equilibrium state $d\Delta P_G/dt = d\Delta P_B/dt = 0$. Using (8), (11), and (12) the following system matrix for the reduced order system is obtained

$$\mathbf{A} = \begin{bmatrix} \frac{-1}{2H}\left(D + \frac{1}{R_G} + \frac{1}{R_B}\right) & \frac{m}{2H} & \frac{-1}{2H} \\ \frac{\alpha}{R_B} & 0 & -\alpha m \\ K_I & 0 & 0 \end{bmatrix}. \tag{15}$$

Fig. 4 depicts the root-loci of the conventional LFC system and the proposed SOC-aware LFC with large values of m, ($m > 4/\alpha$). It is safe to conclude that the reduced-order model is a good approximation of the conventional LFC system.

Therefore, it is correct to use (14) to calculate $K_{I\,crit}$ once m is large enough. For smaller values of m, (14) can be used as an acceptable estimate of $K_{I\,crit}$ and its exact value can be calculated based on the gains of the breaking points of the root

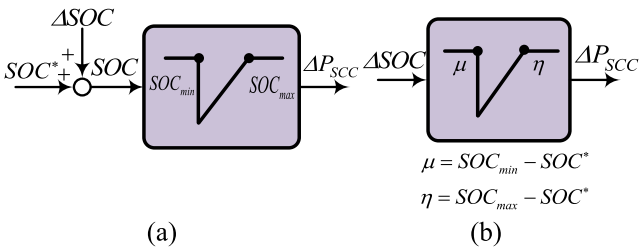

Fig. 5. SCC with (a) SOC as input and (b) ΔSOC as input.

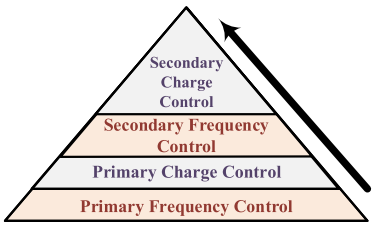

Fig. 6. Hierarchical scheme of the proposed frequency and SOC control.

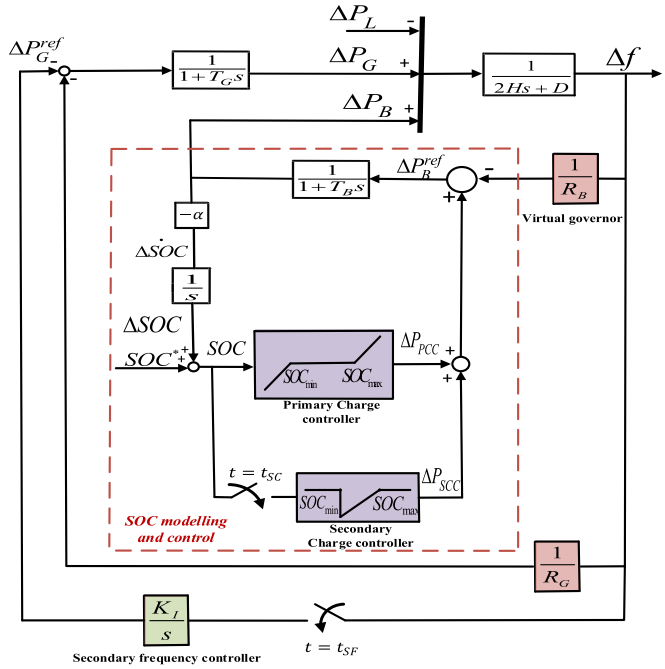

Fig. 7. Proposed SOC-aware hierarchical frequency control.

locus as follows:

$$K_{I\,crit} = \frac{-1}{G(s_b)}, \text{ such that } \frac{d}{ds}K_{I\,crit} = 0. \tag{16}$$

C. Secondary Charge Controller

For enabling the BESS to continue contributing to PFC after it is discharged beyond SOC_{min}, an SCC is designed to be activated during times when there is surplus of power. Fig. 5 shows the block diagram of the proposed SCC, and Fig. 6 demonstrates the hierarchy of the proposed SOC and frequency control scheme. Fig. 7 depicts the proposed frequency and SOC control. As it can be concluded from Fig. 6, t_{SC} in Fig. 7 is larger than t_{SF} since SCC is activated after the SFC. Similar to PCC, SCC is a piecewise linear controller, which modifies the battery reference power as following:

$$\Delta P_{\text{SCC}} = \begin{cases} n(\text{SOC} - \text{SOC}_{\text{max}}) & \text{SOC}_{\text{min}} \le \text{SOC} \le \text{SOC}_{\text{max}} \\ 0 & \text{Otherwise} \end{cases}. \tag{17}$$

This piecewise linear controller, as shown in Fig. 5, is integrated into the proposed SOC-aware frequency control model to complete the hierarchical scheme, as shown in Fig. 7. Discussions about determining the slope n of the linear part are provided in the following section.

The state-space model of the system with SCC is the same as those given in (8)–(12) except for (10), where $\Delta P_{\text{SCC}}/T_B$ will be an additional term. It is worth mentioning that once SCC is activated, which is when SOC lies between SOC_{min} and SOC_{max}, the PCC will not be active, and ΔP_{PCC} will be zero. Thus, the steady-state values of the state variables are achieved using $dx/dt = 0$ for each of the states Δf, ΔP_G, ΔP_B, ΔSOC, and ΔP_G^{ref}. These require that $\Delta f = \Delta P_B = 0, \Delta P_G = \Delta P_L$, and $\text{SOC} = \text{SOC}_{\text{max}}$. The first equation shows that the steady-state error of the frequency response is eliminated, and the BESS does not supply power in the steady state. The second equation shows that the load is met by the generator, and the third equation proves that the SOC reaches its maximum value, meaning that the BESS could be appropriately charged.

D. Stability Analysis

System stability is analyzed using the Popov/circle criterion. As already mentioned, the PCC is not present once the SCC is activated, and thus, its dynamics are not considered in this analysis. For using Popov/circle criterion, the nonlinear element $\Delta P_{\text{SCC}} = f(\Delta\text{SOC})$ must be surrounded by two lines passing through the origin with positive slopes. This implies that the nonlinear element must pass through the origin [31]. However, the SCC does not meet this condition and the equilibrium of the system does not lie at the origin. Thus, the equilibrium of the system is shifted to the origin by defining

$$z = \text{SOC} - \text{SOC}_{\text{max}} = \Delta\text{SOC} - (\text{SOC}_{\text{max}} - \text{SOC}^*) \tag{18}$$

and substituting it in (17), which yields

$$\Delta P_{\text{SCC}} = \begin{cases} 0 & z < \text{SOC}_{\text{min}} - \text{SOC}_{\text{max}} \\ nz & \text{SOC}_{\text{min}} - \text{SOC}_{\text{max}} < z < 0 \\ 0 & z > 0. \end{cases} \tag{19}$$

To use the Popov criterion, the system must be modeled with a transfer function and the nonlinear element in a closed-loop system, as shown in Fig. 8. This transfer function, which must be Hurwitz and finite dimensional [32], [33], is obtained by calculating the state-space matrices A, B, and C from the system dynamics with $-\Delta P_{\text{SCC}}$ as the input and z as the output (as

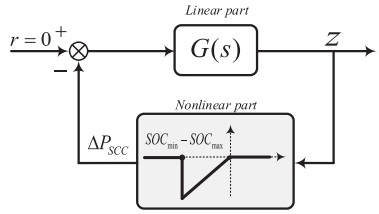

Fig. 8. Nonlinear feedback control block diagram for the Popov/circle criterion.

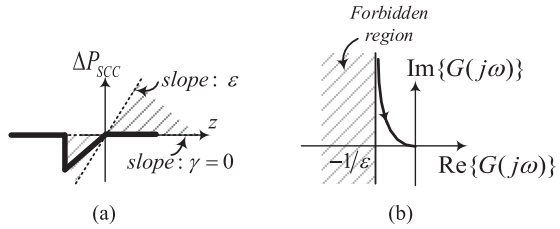

Fig. 9. (a) Nonlinear element sectors for the Popov/circle criterion. (b) Forbidden regions for Popov/circle criterion.

shown in Fig. 8)

$$G(s) = \frac{(-\alpha/T_B)(s^3 + b_2 s^2 + b_1 s + b_0)}{s^5 + a_4 s^4 + a_3 s^3 + a_2 s^2 + a_1 s}. \tag{20}$$

Here are the parameters of (20)

$$b_0 = \frac{K_I}{2HT_G}, \quad b_1 = \frac{1}{2HT_G R_G}, \quad b_2 = \frac{D}{2H} + \frac{1}{T_G}$$

$$a_1 = \frac{K_I}{2HT_G T_B}$$

$$a_2 = \frac{D}{2HT_G T_B} + \frac{1}{2HR_G T_G T_B} + \frac{1}{2HR_B T_G T_B} + \frac{K_I}{2HT_G}$$

$$a_3 = \frac{1}{2HR_G T_G} + \frac{D}{2HT_G} + \frac{D}{2HT_B} + \frac{1}{2HR_B T_B} + \frac{1}{T_G T_B}$$

$$a_4 = \frac{D}{2H} + \frac{1}{T_G} + \frac{1}{T_B}.$$

Recalling the Popov criterion, if $G(s)$ is Hurwitz and satisfies the condition (21), the closed-loop system is absolutely stable, meaning that the origin is asymptotically stable for all nonlinearities existing in the first and third quarter of coordinate so that they pass through the origin. It is worth noting that the transformation (18) leads the proposed nonlinearity to lie between the slopes zero and ε, as shown in Fig. 9(a)

$$\frac{1}{\varepsilon} + Re[G(j\omega)] - \gamma\omega Im[G(j\omega)] > 0. \tag{21}$$

Here, $1/\gamma$ is the slope of the Popov line, and $-1/\varepsilon$ is the intersection of the Popov plot with the real axis. Considering the slope of the Popov line to be infinity, i.e., $\gamma = 0$ leads to the circle criterion as follows [32]:

$$Re[G(j\omega)] > -\frac{1}{\varepsilon}. \tag{22}$$

As the system transfer function $G(s)$ in (20) has a pole at the origin and a negative gain, its Nyquist starts from $-3\pi/2$ and ends at the origin, as shown in Fig. 9(b). As a result, it is obvious that solving $dRe[G(j\omega)]/d\omega = 0$ gives the answer $\omega^* = 0$ rad/s. Thus, using ω^* in (22) leads to the following stability region for n:

$$0 < n < \frac{K_I}{\alpha(K_I T_B + 1/R_G)}. \tag{23}$$

It is clear from (23) that a large α leads to a small n, and from (7), a large α corresponds to a small $E_{\max}$. This means that for a low-capacity BESS, a small n should be selected, similar to m.

The stability region obtained for n in (23) needs to be further refined to count for the maximum allowable frequency deviation ($|\Delta f|_{\max}$). Once the BESS enters charging mode and acts as an active load, the frequency drops, leading to activation of the PFC. Then, the SFC is activated, and the frequency response error is derived to zero. It is reasonable to obtain the frequency drop based on (5), where the load power ΔP_L, will be the power injected to the battery for charging [given in (17)]. Neglecting the PFC transient effect on the BESS output power in charging mode of operation, and keeping in mind that the battery SOC is at its minimum level when it enters charging mode, the following can be written:

$$\Delta f \approx -\frac{\Delta P_L}{D + 1/R_G} \approx \frac{n(\mathrm{SOC}_{\min} - \mathrm{SOC}_{\max})}{D + 1/R_G}$$

$$\Rightarrow n \approx \frac{|\Delta f|_{\max}(D + 1/R_G)}{|\mathrm{SOC}_{\min} - \mathrm{SOC}_{\max}|}. \tag{24}$$

Knowing the maximum allowable frequency deviation, which is usually around 0.5 Hz, the lower and upper bounds of SOC, damping factor and generator droop coefficient, the value for parameter n can be obtained.

IV. Frequency and SOC Control of a Power System With Multiple BESSs

With multiple BESSs, each energy storage unit can be equipped with a PCC and an SCC, and power is shared among them in inverse proportion to their droop gain. In this case, the BESSs SOCs are at different levels and each charge controller functions corresponding with maintaining the SOC within the desired limits. However, if the energy storage units could share their SOC value with each other, SOC-balancing principle [23], [26] could be followed and all the units SOC values would be derived to be equal with each other ($\mathrm{SOC}_1 = \mathrm{SOC}_2 = \ldots = \mathrm{SOC}_{n_{\mathrm{BESS}}}$) in the steady state. In this case, it will be required to equip only one of the units with a PCC and an SCC since other units SOCs will converge to the same amount in the steady state.

For realizing SOC balancing, the mean of the SOC values is calculated and compared with individual BESS SOC values to obtain the error. Each SOC error is then fed to a proportional-integral (PI) controller to produce the BESS reference modifier that derives SOC to the mean value

$$\mathrm{SOC}_{\mathrm{mean}} = \frac{1}{n_{\mathrm{BESS}}} \sum_{i=1}^{n_{\mathrm{BESS}}} \mathrm{SOC}_i \tag{25}$$

$$\Delta P_{\mathrm{SOC_i}} = K_P^{\mathrm{SOC_i}}(\mathrm{SOC}_{\mathrm{mean}} - \mathrm{SOC}_i) + K_I^{\mathrm{SOC_i}} \int (\mathrm{SOC}_{\mathrm{mean}} - \mathrm{SOC}_i). \tag{26}$$

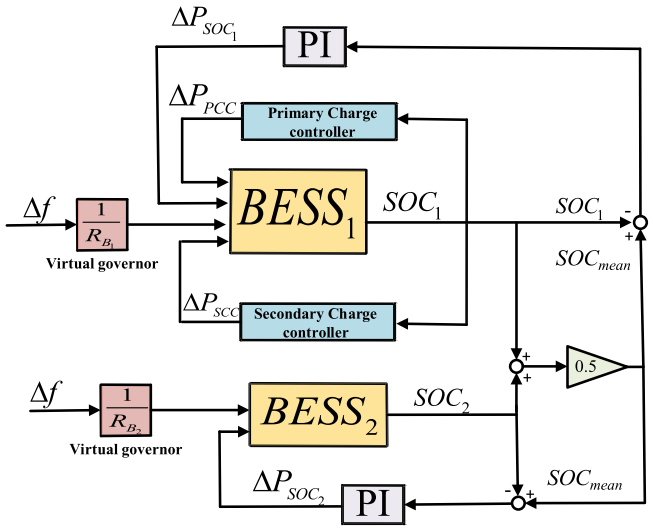

Fig. 10. SOC-balancing strategy for a power system with two BESSs.

Here, n_{BESS} is the number of energy storage units, SOC_i is the SOC of the ith BESS, $K_P^{\text{SOC}_i}$ and $K_I^{\text{SOC}_i}$ are parameters of the SOC-balancing PI controller for the ith BESS, and ΔP_{SOC_i} is the output of the SOC balancing controller, which modifies the BESS reference power. Fig. 10 shows the proposed SOC balancing strategy for a power system with two BESSs.

Guidelines for tuning the PI controllers' parameters can be obtained in [26]. For tuning the PCC and SCC parameters, its reasonable to consider multiple BESSs as one BESS with an equivalent time constant $T_{B_{eq}}$ and droop gain $R_{B_{eq}}$ as follows:

$$\frac{1}{R_{B_{eq}}} = \frac{1}{R_{B_1}} + \frac{1}{R_{B_2}} + \ldots + \frac{1}{R_{B_{n_{\text{BESS}}}}} \tag{27}$$

$$T_{B_{eq}} = \frac{\sum_{i=1}^{n_{\text{BESS}}} T_{B_i}}{n_{\text{BESS}}}. \tag{28}$$

The equivalent droop gain in (27) is obtained using block-diagram principles and approximation conditions in linear systems. With this model approximation, the guidelines for designing PCC and SCC that are discussed in the previous section can be used for tuning their parameters. As how multiple BESSs share power, considering that the SOC-balancing scheme enforces similar SOC dynamics, i.e., $d\text{SOC}_i/dt = d\text{SOC}_j/dt$, (2) and (11) lead to the following:

$$\frac{\Delta P_{B_i}}{\Delta P_{B_j}} = \frac{\alpha_j}{\alpha_i} = \frac{E_{\max_i}}{E_{\max_j}}. \tag{29}$$

This shows that once SOC-balancing scheme is used, the power-sharing among BESSs when the system is under PFC and SCC will be based on their capacities, and not their respective droop gains. As for power sharing between the SG and the equivalent BESS, the droop gain of the equivalent BESS, which is derived in (27), and the droop gain of the SG are the determining factors.

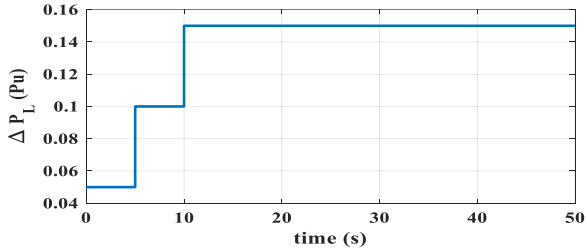

Fig. 11. Increasing load profile.

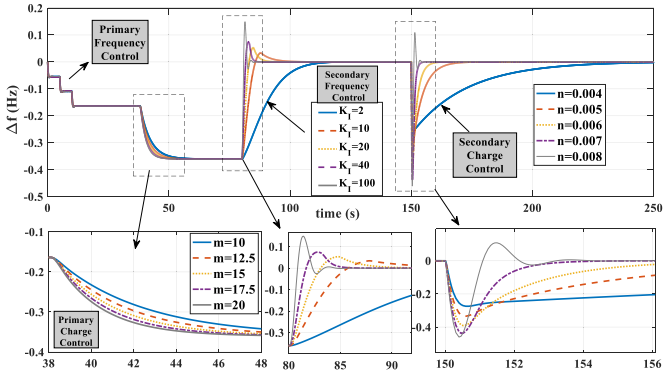

Fig. 12. Grid frequency variation.

V. Model Validation

The proposed SOC-aware frequency control model in Fig. 7 is simulated in MATLAB/SIMULINK to validate its correctness and compatibility with the state-space equations. Simulations are conducted with the following system parameters: $H = 5$ s, $D = 0.8$ p.u., $R_G = 0.05$ p.u., $R_B = 0.04$ p.u., $T_G = 0.2$ s, $T_B = 0.02$ s, $S_{\text{base}} = 200$ kW, $Q_{\max} = 250$ A.h, $v_{b0} = 400$ V, and $E_{\max} = 100$ kW.h. The PCC, SFC, and SCC parameters are varied to illustrate their impact on system performance.

A. Load Increase

Fig. 11 shows the load variation where three 0.05 p.u. step changes are applied at $t = \{0, 5, 10\}$ s. As seen in Fig. 12, at each load increase instance, the system frequency drops. Figs. 13 and 14 depict the BESS and SG power, respectively. It is noteworthy to mention that the BESS and SG share the load power in proportion to the inverse of their droop gains [18]. Fig. 15 shows the SOC; SOC^* is intentionally set to 20.15% to be close to $\text{SOC}_{\min} = 20\%$, so the charge controller becomes activated within the simulation time. This happens at around $t = 38$ s when the PCC manipulates the BESS output power and prevents its further depletion. However, there is a steady-state error in the SOC value, which becomes smaller for larger values of the slope m. This can be explained based on the steady-state SOC relation in (6). Fig. 16 shows the PCC output, confirming that the controller modifies the BESS output power when only $\text{SOC}_{\min}$ is reached. It is seen that the bigger the m is, the faster the controller will act, but this will be at the expense of a higher ROCOF (see Fig. 12). As the BESS output power gradually

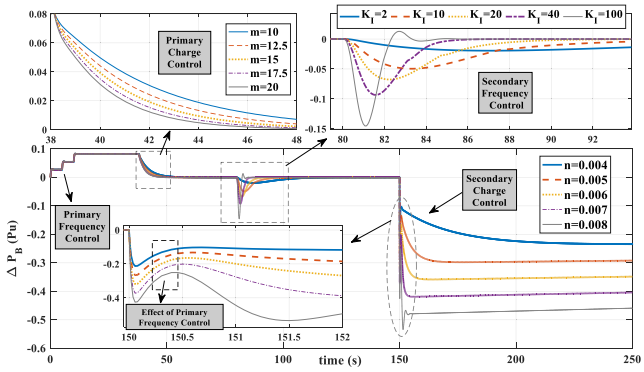

Fig. 13. BESS output power variation.

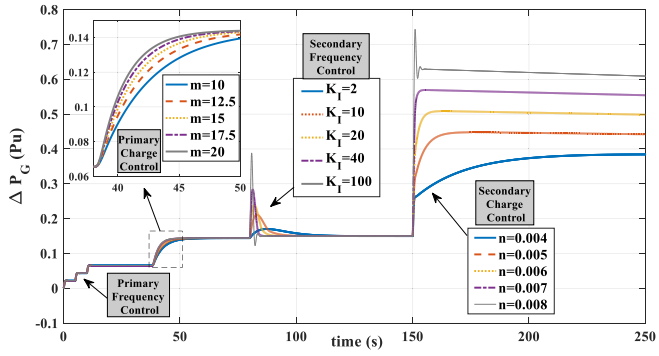

Fig. 14. SG output power variation.

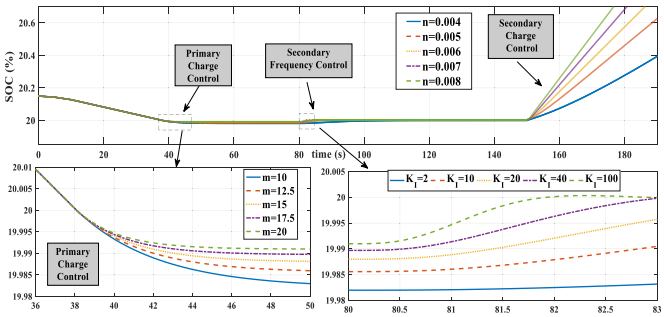

Fig. 15. BESS SOC.

decreases and the frequency drops, the SG ramps up its power to supply the load (see Fig. 14). At $t_{SF} = 80$ s, the SFC loop is closed, restoring the frequency to its nominal value. It is seen in Fig. 12 that the bigger the SFC parameter K_I is, the faster the frequency will be restored, but this translates to a high ROCOF. As seen in Fig. 16, the PCC output becomes zero once the secondary frequency controller is activated. This implies that the PCC is eventually deactivated once the SFC loop is closed. At $t_{SC} = 150$ s, the SCC is activated, and the BESS enters charging mode, leading to frequency drops. But the SG increases its output power to supply the required power.

As seen in Fig. 15, the bigger the n is, the faster SOC increases, and more power is drawn by the BESS. Therefore, the SG needs

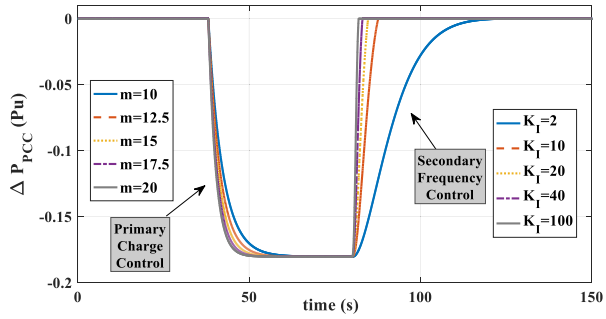

Fig. 16. Primary charge control output.

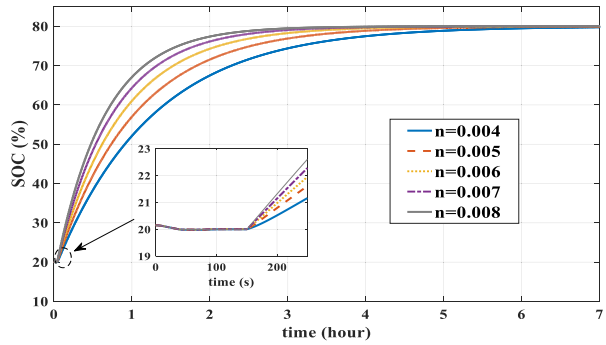

Fig. 17. BESS SOC after seven hours.

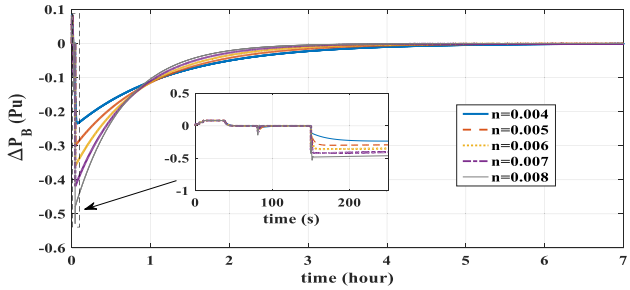

Fig. 18. BESS output power variation after seven hours.

to increase its output power faster, but this will be at the expense of a higher frequency drop.

Simulations were carried out for a longer period to show that after the SCC is activated, the SOC eventually reaches SOC_{max} (which is considered 80%), as can be seen in Fig. 17. The bigger the n is, the faster the SOC reaches its maximum, and the power the BESS draws is higher, as can be observed in Fig. 18. Once $\text{SOC} = \text{SOC}_{\text{max}}$, the BESS ceases drawing power from the SG (see Fig. 18). As seen in Fig. 19, in the steady state, the SG only supplies the load power which is 0.15 p.u. However, during charging mode, it injects more power to the BESS as n increases.

B. Load Decrease

Assuming that SOC reaches $\text{SOC}_{\text{max}} = 80\%$ from the previous load increase scenario, load demand is reduced following the profile shown in Fig. 20. As shown in Figs. 21–24, at each load

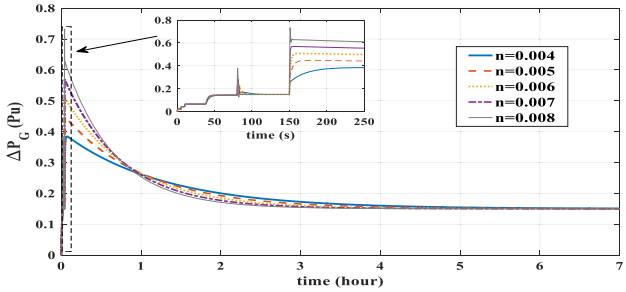

Fig. 19. SG output power variation after seven hours.

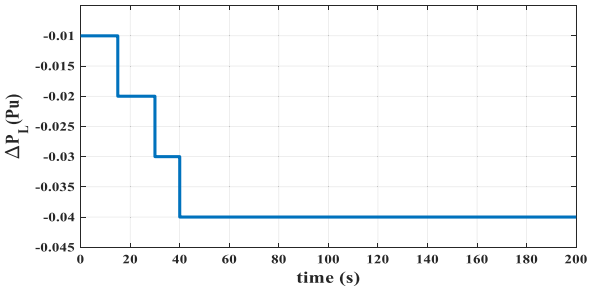

Fig. 20. Decreasing load profile.

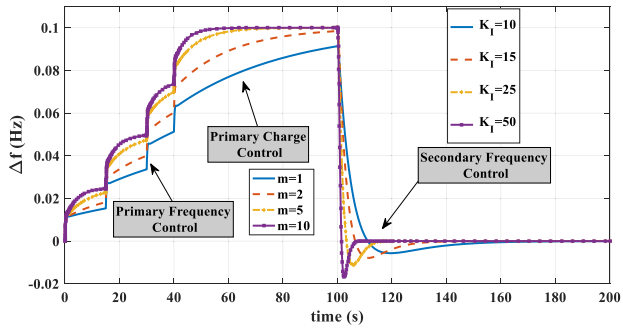

Fig. 21. Grid frequency variation.

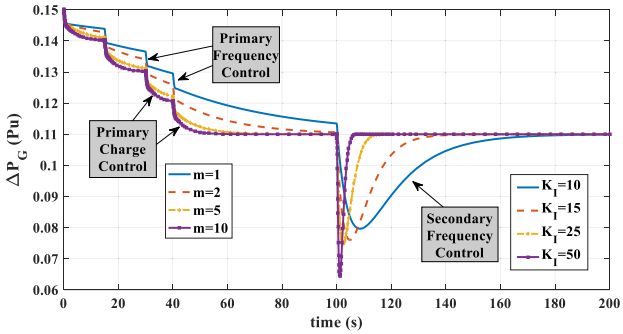

Fig. 22. SG output power variation.

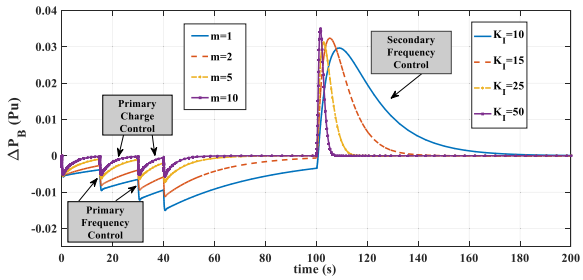

Fig. 23. BESS output power variation.

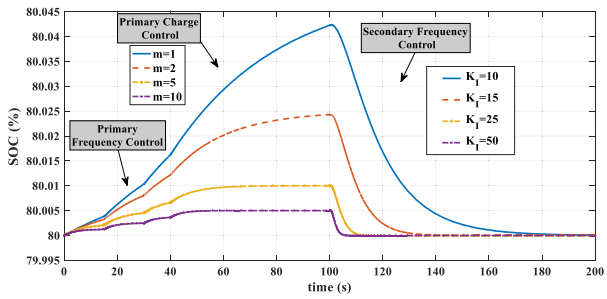

Fig. 24. BESS SOC.

decrease instance, the grid frequency goes up due to a decrease in the SG output power. The BESS output power also decreases and becomes negative, meaning that the BESS enters charging mode, leading to an increase in its SOC. This activates the PCC, which derives the BESS power to zero as it aims at maintaining SOC at SOC_{max}. Like the load increase scenario, the SOC steady-state error is eliminated once the SFC loop is closed, and the frequency settles at the rated value, with the BESS and SG power variations settling at zero and the corresponding value for maintaining the rated frequency, respectively.

C. Comparative Studies

Comparative studies are conducted against the method proposed in [20], where the BESS is charged in the constant current mode and once the lower/upper bounds of SOC are reached, the *d*-axis reference current of the inverter is set to zero (where here, equivalently the BESS reference power is set to zero) to prevent BESS from discharging/charging beyond the allowable limits. As seen in Figs. 25 and 26, although the method in [20] leads to zero SOC steady-state error, the abrupt cease of current draw/injection from/to the BESS leads to larger frequency deviations and ROCOF. This confirms the advantage of our proposed method, where SOC is integrated into the system dynamics and the LFC system is designed by taking SOC into consideration.

VI. HIL Results

The BESS-SG system shown in Fig. 27 is modeled on a HIL setup to verify real-time implementation feasibility of the proposed hierarchical SOC and frequency control scheme. Only the load increase scenario of the model validation section is examined in HIL results to confirm the validity of simulation results. The entire system, including the BESS, SG, loads, and interfacing power electronic converters, are modeled on an OP4510 real-time simulator using Simulink blocks with a time step of 50 μs, while the inverter control is implemented on a TI TMS320F28335 DSP. The BESS block in Simulink is

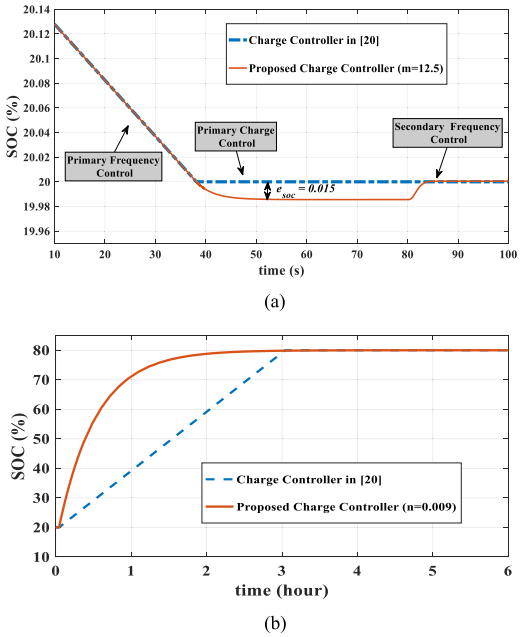

Fig. 25. BESS SOC. (a) Discharging mode reaching SOC_{min}. (b) Charging mode reaching SOC_{max}.

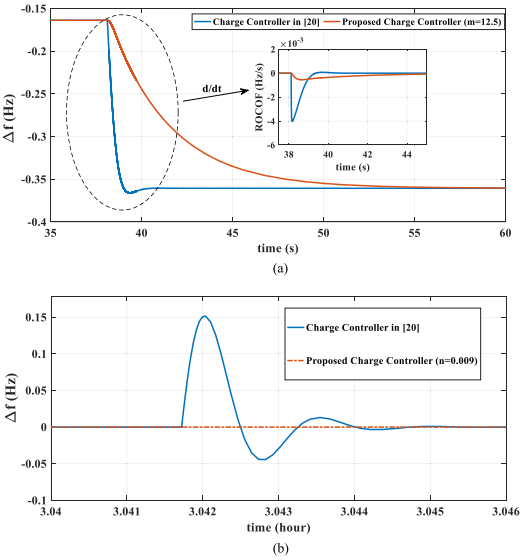

Fig. 26. Grid frequency variation. (a) Discharging mode reaching SOC_{min}. (b) Charging mode reaching SOC_{max}.

based on an aging model and considers different parameters, such as ambient temperature, capacity and internal resistance at end of life. It also provides BESS SOC, current, and voltage as measurable signals.

The BESS inverter is controlled using the PQ strategy to track the BESS reference power (determined through the proposed method) and inject/absorb the desired power. The BESS dc–dc converter controls the dc-link voltage at its reference set point. Both converters switching frequency is set at 10 kHz. The system parameters are like those used in model validation with $m = 10$, $n = 0.002$, $\text{SOC}_{\text{max}} = 80\%$, $\text{SOC}^* = 20.1\%$ and $v_{\text{dc}}^{ref} = 800$ V. The BESS dc-link capacitor (C_{dc}), filter inductance (L_f), and the line inductance (L_{line}) values are 1 mF and 0.6 mH, and 1 mH, respectively. The BESS voltage loop PI controller parameters are $K_P^V = 0.85$, $K_I^V = 10$, the BESS current loop PI controller parameters are $K_P^C = 0.01$, $K_I^C = 10$, and the inverter current loop PI parameters are $K_P^i = 25$, $K_I^i = 500$.

The SFC loop is closed at $t_{SF} = 30$ s, and the SCC is activated at $t_{SC} = 60$ s. The load profile is similar to Fig. 11. The results of Figs. 28–31 confirm those obtained using the state-space equations in the previous section. At each load increase instance, the system frequency drops. Once the SOC reaches $\text{SOC}_{\text{min}} = 20\%$, the PCC becomes activated and halts power draw from the BESS, triggering the SG to ramp up its generation to supply the load. When the SFC loop is closed, frequency is restored to its nominal value.

After the SCC is activated, the BESS draws power from the SG to be charged. Fig. 32 shows the dc-link voltage which drops momentarily at each load increase instance due to discharge of the dc-link capacitor; however, the dc–dc converter control loop compensates for this drop by drawing current from the BESS (see Fig. 33). As seen in Fig. 34, the battery voltage drop at load increase instances is very negligible (∼0.3 v). Once the PCC is applied, the dc-link voltage increases due to the decrease in the BESS power, and the BESS current decreases to zero, but the BESS voltage increases as it ceases discharging. Once the SFC loop is closed, the dc-link voltage slightly increases as the BESS is charged by drawing current (see Fig. 33) to compensate for the SOC error. Also, the BESS voltage increases slightly due to this short charge period. After the SCC is activated, the BESS starts drawing power to charge. Therefore, its current switches direction and its voltage continues to increase.

SOC-balancing with two BESSs is validated with HIL studies, as well. The BESS control strategy in Fig. 10 is used in the BESS-SG system in Fig. 27. The load profile is based on Fig. 11. The time constants of the BESSs are set to $T_{B_1} = 0.02$ s and $T_{B_2} = 0.08$ s, and their droop gains are set to $R_{B_1} = 0.03$ p.u. and $R_{B_2} = 0.06$ pu. The PCC, SFC, and SCC parameters are set to $m = 10$, $K_I = 20$, and $n = 0.002$, respectively. The SOC-balancing PI parameters are set as $K_P^{\text{SOC}_1} = K_P^{\text{SOC}_2} = K_I^{\text{SOC}_1} = K_I^{\text{SOC}_2} = 3$. The initial SOCs are intentionally set as $\text{SOC}_1 = 20.2\%$ and $\text{SOC}_2 = 20.1\%$ to enforce activation of the PCC, and also show the convergence of SOCs to a mean value after starting off at different values.

To show the impact of the BESSs capacity on power sharing, two cases are considered: in the first case, both the BESS capacities are set to 100 kWh, and in the second case, they are set to 100 kWh and 200 kWh. Fig. 35 depicts the BESSs output powers for the first case. It is seen that both the BESSs produce the same power after some oscillations despite having different droop gains. However, for the second case, it is seen in Fig. 36 that the BESSs produce power in proportion to their capacities when the system is under PFC and SCC hierarchy levels. This confirms what was derived in (29). Fig. 37 shows the BESSs SOC under the SOC-balancing scheme. As there are two BESSs in the system ($n_{\text{BESS}} = 2$), it can be assumed that one BESS with an equivalent time constant and droop gain produces

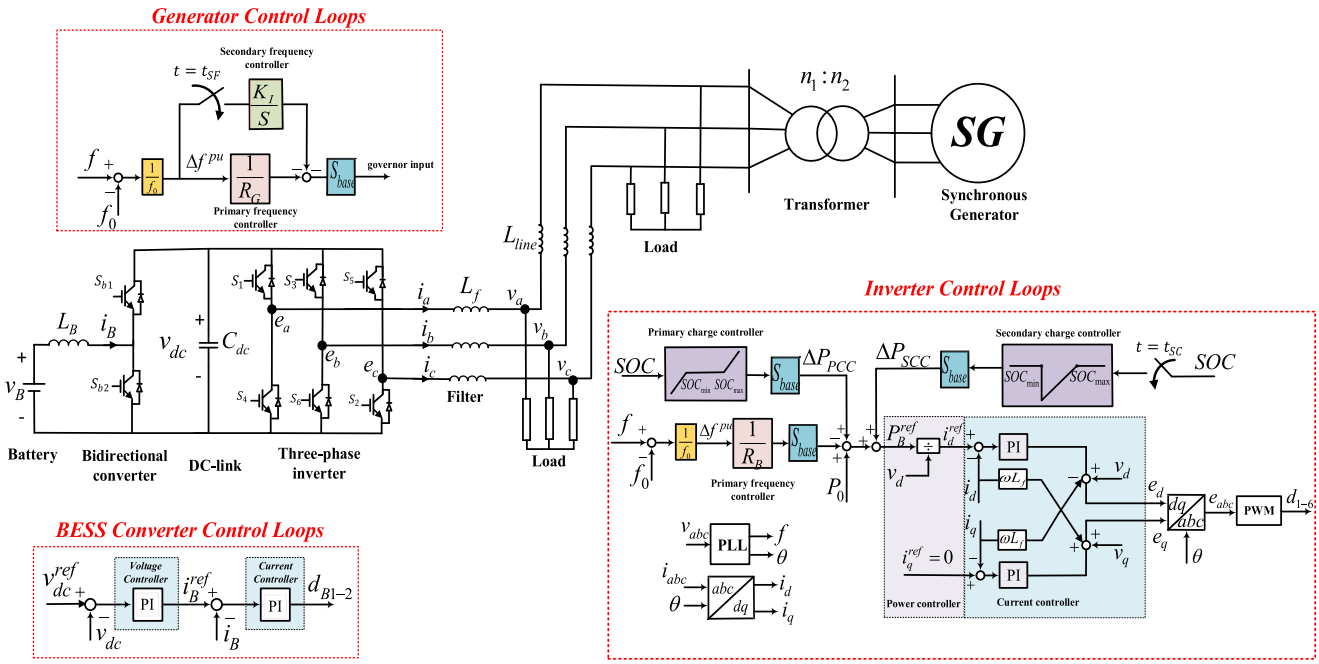

Fig. 27. Schematic of the BESS-SG system for HIL studies.

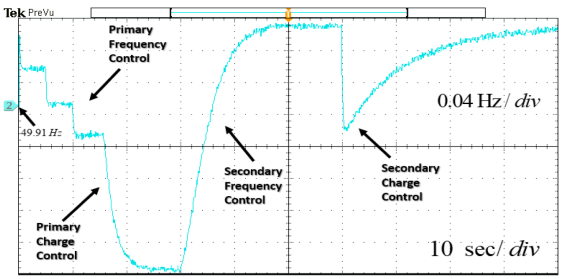

Fig. 28. Grid frequency.

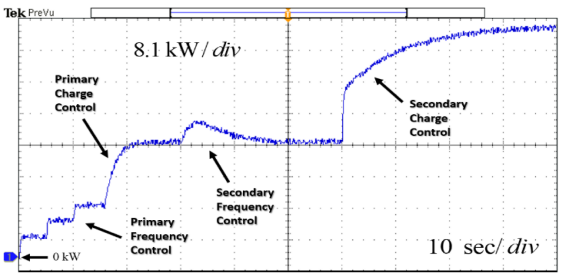

Fig. 29. SG output power.

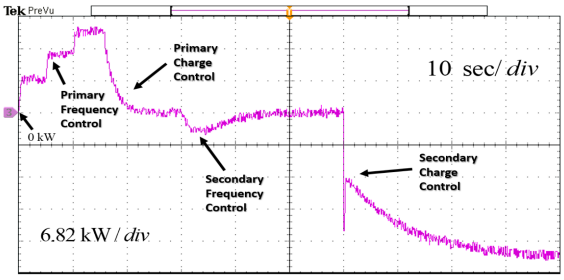

Fig. 30. BESS output power.

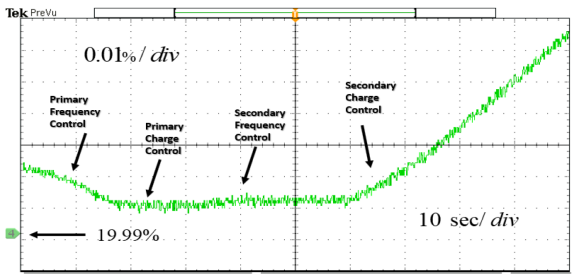

Fig. 31. BESS SOC.

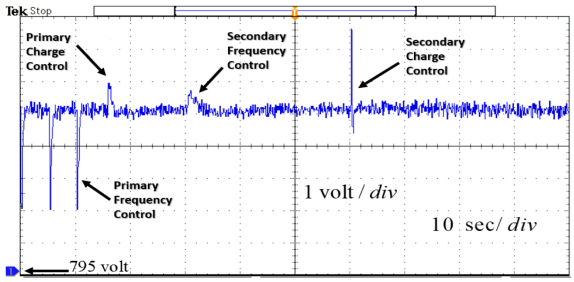

Fig. 32. DC-link voltage.

summation of the power levels in Figs. 35 or 36, and power is shared between that equivalent BESS and the SG in proportion to inverse of their respective droop gains. It is notable that the grid frequency and SG output power are not affected by SOC balancing and remain similar to those illustrated in Figs. 28 and 29, respectively.

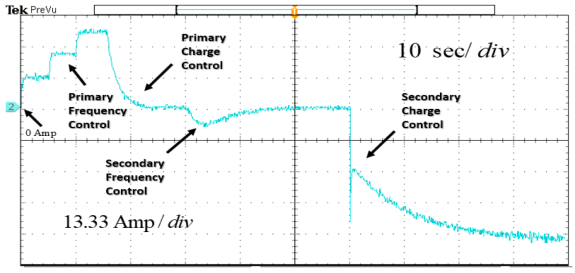

Fig. 33. BESS current.

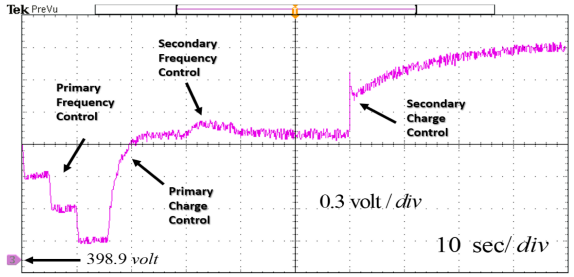

Fig. 34. BESS voltage.

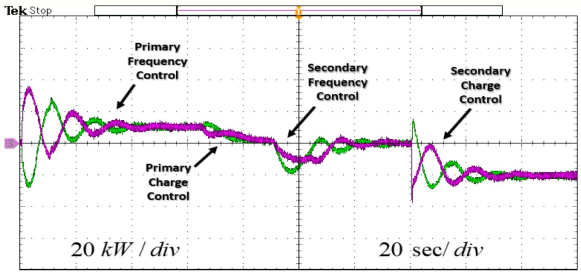

Fig. 35. BESSs output powers under SOC-balancing with different droop gains but with same capacities.

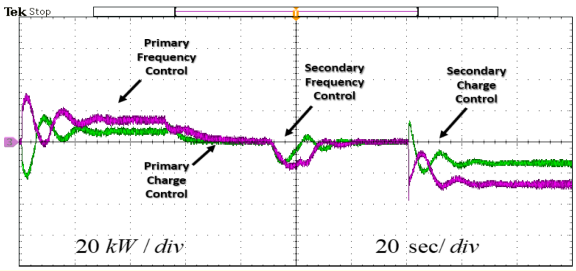

Fig. 36. BESSs output powers under SOC-balancing with different capacities.

VII. Conclusion

A hierarchical SOC and frequency control scheme is proposed for power systems with battery energy storage systems. The proposed control scheme is based on the state-space model of the system and is in closed form thanks to a relation derived between the BESS SOC and power variation. On top of the PFC, a PCC is designed and employed to prohibit BESS discharge/charge beyond the minimum/maximum allowable SOC.

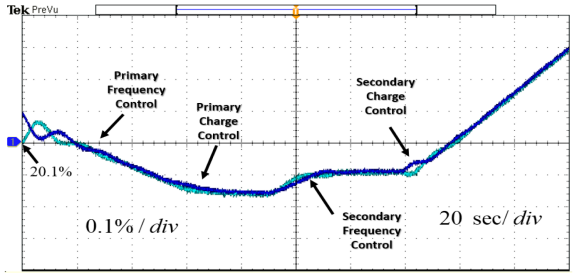

Fig. 37. BESSs SOC under SOC-balancing.

A similar piecewise SCC is designed to be activated following the secondary frequency controller to charge the BESS to its maximum allowable SOC at off-peak load intervals. Selecting the PCC and SCC parameters are based on the Popov/circle stability criterion.

The proposed hierarchical SOC and frequency control is then extended to a power system with multiple BESSs. It is shown that by relying on communicating SOC values among the energy storage units, the SOC-balancing strategy can be implemented, and by equipping only one of the units with the proposed charge controllers, SOC of all the other BESSs can be controlled by simple PI controllers.

The validity of the model derived based on the system state-space equations is confirmed through simulations. Those results also show that larger values of the PCC, SFC, and SCC parameters provide faster frequency response, but at the expense of a higher ROCOF. HIL simulation results, with one and multiple BESSs, confirm real-time implementation feasibility of the proposed control and its effectiveness in stable control of grid frequency under different load and BESS SOC conditions.

References

[1] J. Fang, H. Li, Y. Tang, and F. Blaabjerg, "On the inertia of future more-electronics power systems," *IEEE J. Emerg. Sel. Topics Power Electron.*, vol. 7, no. 4, pp. 2130–2146, Dec. 2019.

[2] V. Gholamrezaie, M. G. Dozein, H. Monsef, and B. Wu, "An optimal frequency control method through a dynamic load frequency control (LFC) model incorporating wind farm," *IEEE Syst. J.*, vol. 12, no. 1, pp. 392–401, Mar. 2018.

[3] M.-H. Khooban, T. Dragicevic, F. Blaabjerg, and M. Delimar, "Shipboard microgrids: A novel approach to load frequency control," *IEEE Trans. Sustain. Energy*, vol. 9, no. 2, pp. 843–852, Apr. 2018.

[4] M.-H. Khooban, "Secondary load frequency control of time-delay stand-alone microgrids with electric vehicles," *IEEE Trans. Ind. Electron.*, vol. 65, no. 9, pp. 7416–7422, Sep. 2018.

[5] M. Khan, H. Sun, Y. Xiang, and D. Shi, "Electric vehicles participation in load frequency control based on mixed H2/H∞," *Int. J. Elect. Power Energy Syst.*, vol. 125, 2021, Art. no. 106420.

[6] S. A. Hosseini, M. Toulabi, A. S. Dobakhshari, A. Ashouri-Zadeh, and A. M. Ranjbar, "Delay compensation of demand response and adaptive disturbance rejection applied to power system frequency control," *IEEE Trans. Power Syst.*, vol. 35, no. 3, pp. 2037–2046, May 2020.

[7] X.-C. Shangguan et al., "Robust load frequency control for power system considering transmission delay and sampling period," *IEEE Trans. Ind. Informat.*, vol. 17, no. 8, pp. 5292–5303, Aug. 2021.

[8] N. Vafamand, M. H. Khooban, T. Dragičević, J. Boudjadar, and M. H. Asemani, "Time-delayed stabilizing secondary load frequency control of shipboard microgrids," *IEEE Syst. J.*, vol. 13, no. 3, pp. 3233–3241, Sep. 2019.

[9] H. Bevrani, M. R. Feizi, and S. Ataee, "Robust frequency control in an islanded microgrid: H-and $\mu $-synthesis approaches," *IEEE Trans. Smart Grid*, vol. 7, no. 2, pp. 706–717, Mar. 2016.
[10] S. Hu, X. Ge, X. Chen, and D. Yue, "Resilient load frequency control of islanded AC microgrids under concurrent false data injection and denial-of-service attacks," *IEEE Trans. Smart Grid*, vol. 14, no. 1, pp. 690–700, Jan. 2023.
[11] M. R. Khalghani, J. Solanki, S. K. Solanki, M. H. Khooban, and A. Sargolzaei, "Resilient frequency control design for microgrids under false data injection," *IEEE Trans. Ind. Electron.*, vol. 68, no. 3, pp. 2151–2162, Mar. 2021.
[12] T. Amraee, M. G. Darebaghi, A. Soroudi, and A. Keane, "Probabilistic under frequency load shedding considering RoCoF relays of distributed generators," *IEEE Trans. Power Syst.*, vol. 33, no. 4, pp. 3587–3598, Jul. 2018.
[13] Y. Han, P. M. Young, A. Jain, and D. Zimmerle, "Robust control for microgrid frequency deviation reduction with attached storage system," *IEEE Trans. Smart Grid*, vol. 6, no. 2, pp. 557–565, Mar. 2015.
[14] H. Bevrani, F. Habibi, P. Babahajyani, M. Watanabe, and Y. Mitani, "Intelligent frequency control in an AC microgrid: Online PSO-based fuzzy tuning approach," *IEEE Trans. Smart Grid*, vol. 3, no. 4, pp. 1935–1944, Dec. 2012.
[15] I. Pan and S. Das, "Kriging based surrogate modeling for fractional order control of microgrids," *IEEE Trans. Smart Grid*, vol. 6, no. 1, pp. 36–44, Jan. 2015.
[16] A. Rafiee, Y. Batmani, F. Ahmadi, and H. Bevrani, "Robust load-frequency control in islanded microgrids: Virtual synchronous generator concept and quantitative feedback theory," *IEEE Trans. Power Syst.*, vol. 36, no. 6, pp. 5408–5416, Nov. 2021.
[17] A. Fathi, Q. Shafiee, and H. Bevrani, "Robust frequency control of microgrids using an extended virtual synchronous generator," *IEEE Trans. Power Syst.*, vol. 33, no. 6, pp. 6289–6297, Nov. 2018.
[18] Z. Afshar, M. M. Zadeh, S. M. T. Bathaee, and G. Gharehpetian, "Primary and secondary frequency control of low-inertia microgrids with battery energy storage and intermittent renewable energy resources," in *Proc. 11th Power Electron., Drive Syst., Technol. Conf.*, 2020, pp. 1–6.
[19] P. Li, Z. Tan, Y. Zhou, C. Li, R. Li, and X. Qi, "Secondary frequency regulation strategy with fuzzy logic method and self-adaptive modification of state of charge," *IEEE Access*, vol. 6, pp. 43575–43585, 2018.
[20] U. Datta, A. Kalam, and J. Shi, "Battery energy storage system control for mitigating PV penetration impact on primary frequency control and state-of-charge recovery," *IEEE Trans. Sustain. Energy*, vol. 11, no. 2, pp. 746–757, Apr. 2020.
[21] C. Mu, Y. Zhang, H. Jia, and H. He, "Energy-storage-based intelligent frequency control of microgrid with stochastic model uncertainties," *IEEE Trans. Smart Grid*, vol. 11, no. 2, pp. 1748–1758, Mar. 2020.
[22] S. Sitompul, Y. Hanawa, V. Bupphaves, and G. Fujita, "State of charge control integrated with load frequency control for BESS in islanded microgrid," *Energies*, vol. 13, no. 18, 2020, Art. no. 4657.
[23] C. Li, E. A. A. Coelho, T. Dragicevic, J. M. Guerrero, and J. C. Vasquez, "Multiagent-based distributed state of charge balancing control for distributed energy storage units in AC microgrids," *IEEE Trans. Ind. Appl.*, vol. 53, no. 3, pp. 2369–2381, May/Jun. 2017.
[24] H. Liu, Z. Hu, Y. Song, and J. Lin, "Decentralized vehicle-to-grid control for primary frequency regulation considering charging demands," *IEEE Trans. Power Syst.*, vol. 28, no. 3, pp. 3480–3489, Aug. 2013.
[25] Z. Tan, X. Li, L. He, Y. Li, and J. Huang, "Primary frequency control with BESS considering adaptive SoC recovery," *Int. J. Elect. Power Energy Syst.*, vol. 117, 2020, Art. no. 105588.
[26] S. V. M. Ouoba, A. Houari, and M. Machmoum, "Resilient control for distributed energy storage units in an islanded AC microgrid," *IEEE J. Emerg. Sel. Topics Power Electron.*, vol. 12, no. 2, pp. 1446–1455, Apr. 2024.
[27] O. Palizban and K. Kauhaniemi, "Distributed cooperative control of battery energy storage system in AC microgrid applications," *J. Energy Storage*, vol. 3, pp. 43–51, 2015.
[28] S. Zhang, Y. Mishra, and M. Shahidehpour, "Fuzzy-logic based frequency controller for wind farms augmented with energy storage systems," *IEEE Trans. Power Syst.*, vol. 31, no. 2, pp. 1595–1603, Mar. 2016.
[29] Z. Afshar, H. Rahmanei, I. Bhogaraju, and M. Farasat, "SOC-aware primary frequency control of low-inertia power systems with battery energy storage," in *Proc. IEEE Texas Power Energy Conf.*, 2023, pp. 1–6.
[30] D. Chaturvedi, P. Satsangi, and P. Kalra, "Load frequency control: A generalised neural network approach," *Int. J. Elect. Power Energy Syst.*, vol. 21, no. 6, pp. 405–415, 1999.
[31] J.-J. E. Slotine and W. Li, *Applied Nonlinear Control*. Hoboken, NJ, USA: Prentice-Hall, 1991.
[32] H. K. Khalil, *Nonlinear Systems*, 3rd ed. Hoboken, NJ, USA: Prentice-Hall, 2002.
[33] G. Zames, "On the input-output stability of time-varying nonlinear feedback systems part one: Conditions derived using concepts of loop gain, conicity, and positivity," *IEEE Trans. Automat. Control*, vol. 11, no. 2, pp. 228–238, Apr. 1966.

Zakaria Afshar (Student Member, IEEE) received the M.Sc. degree in electrical power engineering from K. N. Toosi University of Technology, Tehran, Iran, in 2018. He is currently working toward the Ph.D. degree in electrical engineering with Louisiana State University, Baton Rouge, LA, USA.

His current research interests include microgrid dynamics and control, low-inertia power systems, and control of power grids with battery energy storage systems.

Indra Bhogaraju received the Ph.D. degree in electrical engineering from Louisiana State University, Baton Rouge, LA, USA, in 2023.

He is currently a Scientist with ABB Corporate Research Center, Raleigh, NC, USA. His research interest includes nonlinear control and its application to renewable energy and hybrid energy storage systems.

Hamid Rahmanei received the B.S. and M.Sc. degrees in mechanical engineering in 2013 and 2016, respectively, both from K. N. Toosi University of Technology, Tehran, Iran, where he is currently working toward the Ph.D. degree.

His research interests include dynamic systems, vehicle dynamics and control, and nonlinear vibrations.

Mehdi Farasat (Senior Member, IEEE) received the Ph.D. degree in electrical engineering from the University of Nevada, Reno, Nevada, in 2014.

He is currently an Associate Professor with the School of Electrical Engineering and Computer Science, Louisiana State University, Baton Rouge, LA, USA. His research interests include design, modeling, and control of power electronics converters in renewable energy and electrified transportation systems.